Journal of Power Sources 196 (2011) 8625–8631

Contents lists available at ScienceDirect

Journal of Power Sources

journal homepage: www.elsevier.com/locate/jpowsour

$Li(Ni_{0.40}Mn_{0.40}Co_{0.15}Al_{0.05})O_2$: A promising positive electrode material for high-power and safe lithium-ion batteries

J. Bains[a,b], L. Croguennec[a,b], J. Bréger[c,*], F. Castaing[c], S. Levasseur[d], C. Delmas[a,b], Ph. Biensan[c]

[a] CNRS, Université de Bordeaux, ICMCB, 87 av. Schweitzer, Pessac, F-33608, France
[b] IPB, ENSCBP, ICMCB, Pessac, F-33608, France
[c] SAFT, Direction de la Recherche, 111-113 Bld Alfred Daney, Bordeaux, F-33074, France
[d] UMICORE Research & Development, Kasteelstraat 7, B-2250 Olen, Belgium

ARTICLE INFO

Article history:
Received 17 January 2011
Received in revised form 6 May 2011
Accepted 3 June 2011
Available online 12 June 2011

Keywords:
Lithium-ion battery
Positive electrode material
Layered oxide
Aluminium substitution
X-ray diffraction
Power electrochemical performance
Thermal stability

ABSTRACT

$Li_{1.11}(Ni_{0.40}Mn_{0.39}Co_{0.16}Al_{0.05})_{0.89}O_2$ was synthesized through coprecipitation of a mixed hydroxide followed by calcination with $LiOH{\cdot}H_2O$ during 10 h at 500 °C and 950 °C. Electrochemical tests and their comparison with those obtained for an industrial $Li(Ni_{1-y-z}Co_yAl_z)O_2$ material reveal that $Li_{1.11}(Ni_{0.40}Mn_{0.39}Co_{0.16}Al_{0.05})_{0.89}O_2$ shows good charge–discharge performance, even at high rate according to a protocol well established by car-makers for testing power abilities of batteries for electric and hybrid electric vehicles. In addition, this material shows a significant improvement in thermal stability in the highly deintercalated state (charged state of the battery) over the industrial material. Equivalent (or higher) energy and power densities with a significantly greater thermal stability make of $Li_{1.11}(Ni_{0.40}Mn_{0.39}Co_{0.16}Al_{0.05})_{0.89}O_2$ an interesting candidate as positive electrode material for large lithium-ion batteries.

1. Introduction

During the past decade, rechargeable lithium batteries have been much investigated and widely used because they potentially have a large range of applications [1]; they are not only required to enable the fairly charge/discharge rates applications like mobile phone and portable computer but also to meet an increasing need for new applications such as electric vehicles (EV) or hybrid electric vehicles (HEV) [2]. Unlike most of the applications, where the energy density or the capacity of the batteries is the most relevant concern, HEV applications require batteries with high power. The cell capacity is related to the amount of active lithium ions that are able to shuttle between the positive and negative electrodes under the operating conditions, while the power of a cell is directly related to the cell impedance or internal resistance [3]. More importantly, for battery applications the capacity fade is not necessarily associated with a power fade, and vice versa. Therefore, it is essential to develop lithium-ion batteries with small and stable cell impedance [4].

$LiCoO_2$ shows high energy density and cycling stability that make it an excellent positive electrode candidate for batteries used in portable applications, but it has also some disadvantages such as poor thermal stability, inferior overcharge characteristics and toxicity. Since the newly developed EV and HEV require high volumetric energy density and thermal stability over those of $LiCoO_2$ it accelerates intensive researches to find an alternative positive electrode material for high energy applications. For instance, since the pioneering work of Goodenough et al. [5], olivine $LiFePO_4$ positive electrode materials were shown to exhibit excellent overcharge characteristics and good chemical and thermal stability [6], with low toxicity and low cost, which make them particularly attractive for high-power applications. The main drawback of $LiFePO_4$ remains its low discharge potential (3.45 V *vs.* Li^+/Li) that limits the energy density delivered by this material (15% less than for $LiCoO_2$). In fact, its low ionic and electronic conductivities at first very detrimental to good transport properties were overcome by forming carbon coated nanomaterials [7].

Layered lithium nickel manganese oxides are also promising and inexpensive alternative positive electrode materials to the commercial $LiCoO_2$ electrode materials used in most of the lithium-ion batteries. Among these, $LiNi_{0.5}Mn_{0.5}O_2$ shows quite low Li diffusivity and thus charge/discharge rates because of the high ratio of Ni cations present in the Li layers [8,9], making it not satisfying the high power requirements in HEV applications. Recently, an other layered transition metal oxide, $Li(Ni_{1/3}Co_{1/3}Mn_{1/3})O_2$, was introduced by Ohzuku and Makimura [10] as a good candidate as positive

* Corresponding author. Tel.: +33 5 5710 6899, fax: +33 5 5710 6414.
E-mail address: Julien.Breger@saftbatteries.com (J. Bréger).

0378-7753/$ – see front matter © 2011 Elsevier B.V. All rights reserved.
doi:10.1016/j.jpowsour.2011.06.016

electrode material to replace $LiCoO_2$. This material attracts significant interest for a few years now because, due to a combination of nickel, manganese and cobalt, it possesses large specific capacity (more than 200 mAh g^{-1}) within the voltage range of 2.5–4.6 V *vs.* Li^+/Li, with a lower cost and less toxicity than $LiCoO_2$. It makes it very promising for use as the positive electrode in lithium-ion batteries [4,11–13].

Some of us have been working for a long time now on the understanding of the mechanisms involved upon cycling of layered $LiNi_{1-y-z}Co_yAl_zO_2$ (denoted as NCA in the following with $z < y < 0.20$) [14] or $LiNi_xMn_yCo_zO_2$ as positive electrode material [15,16] in Li-ion cells. The results discussed in this paper are part of a patent [17] and will show that partial substitution of aluminium for cobalt in a nickel and manganese rich layered oxide "$Li(Ni_{0.40}Mn_{0.40}Co_{0.15}Al_{0.05})O_2$" can combine excellent thermal stability with promising electrochemical performance (both in capacity and power) as also recently shown for other compositions by Dahn et al. [18,19]. A comparison with an industrial NCA material will be also given here.

2. Experimental

"$Li(Ni_{0.40}Mn_{0.40}Co_{0.15}Al_{0.05})O_2$" was prepared following the "mixed hydroxide" method reported by Ohzuku et al. [8] and Lu et al. [20]. The first step of the synthesis consisted in the formation of "mixed hydroxides" (M = Ni, Mn, Co and Al) using the coprecipitation route. A mixed (1 M) aqueous solution of $Ni(NO_3)_2{\cdot}6H_2O$ (98% Sigma Aldrich), $Mn(NO_3)_2{\cdot}4H_2O$ (98% Prolabo), $Co(NO_3)_2{\cdot}6H_2O$ (98% Sigma Aldrich) and $Al(NO_3)_3{\cdot}9H_2O$ (98% Sigma–Aldrich) prepared with the [Ni/Mn/Co/Al]:[40/40/15/5] molar ratio, was added dropwise into a basic solution (LiOH in excess (98% Sigma–Aldrich)) under magnetic stirring. A green–brown "mixed hydroxide" precipitated. The resulting precipitate was filtrated, washed with deionised water and dried overnight in an oven at 180 °C. The second step consisted in the addition of $LiOH{\cdot}H_2O$ powder and in mixing in an agate mortar with the precipitate. The nominal Li/M ratio was adjusted to 1.08 to compensate for lithium loss due to the high temperature of the synthesis. Then, the mixture was pressed as pellets, heated overnight in air at 500 °C to decompose nitrates and quenched in liquid nitrogen. Finally, after a grinding step, the mixture was pressed again as pellets, calcinated in air at 950 °C overnight and quenched in liquid nitrogen, before a final grinding step.

In order to confirm the chemical composition of this sample, lithium, aluminium and transition metal ions were titrated using ICP-OES measurements (Varian 720-ES), whereas C and H were analyzed by gas chromatography performed with a Thermo Fisher Flash EA1112 CHNS analyzer. Powder X-ray diffraction (XRD) analyses were performed using a Siemens D5000 diffractometer and Cu Kα radiation (λ = 1.5406 Å). For structural study using the Rietveld method [21], data were collected in the 5–120° (2θ) range with steps of 0.02° (2θ) and a constant counting time of 8 s before being analyzed using the Fullprof program [22]. Magnetic measurements were carried out with a Superconducting Quantum Interface Device (quantum design MPMS-5S). Magnetization *vs.* field plots were recorded at 5 K over the [−50 kOe; +50 kOe] range. The H/M ratio (H applied field of 10 kOe and M measured magnetization) was measured in the [5–300 K] temperature range. High resolution scanning electronic microscopy (SEM) analysis of the samples was performed using a Hitachi S-4500 microscope. Powders were metallized by palladium plasma.

First electrochemical characterizations were performed in coin cells at room temperature with lithium foil as negative electrode. The positive electrode was cast on an aluminium foil as a mixture of the active material "$Li(Ni_{0.40}Mn_{0.40}Co_{0.15}Al_{0.05})O_2$" with carbon black/graphite (1:1) (as additives for an improved porosity and electronic conductivity) and polyvinylidene fluoride (PVDF) (as binder). The electrolyte solution was $LiPF_6$ (1 M) in a mixture of ethylene carbonate (EC), propylene carbonate (PC) and dimethyl carbonate (DMC) in volume proportions 1:1:3. Cells were assembled in an argon-filled dry box and then cycled between 2.0 and 4.5 V *vs.* Li^+/Li, in galvanostatic mode at $C/10$ rate (C corresponding to the nominal capacity of 180 mAh g^{-1}).

Then, power tests were performed in industrial laboratory in wound 4/5A-type cells. The negative electrode was a graphite mixture coated on a copper foil as current collector. The positive electrodes (mixture of 83% active material, 12% carbon and 5% PVDF binder) were cast on an aluminium foil as current collector. The positive and negative electrode loadings corresponded to power loadings (around 6 mg cm^{-2} per side and 4 mg cm^{-2} per side for positive and negative, respectively). The electrolyte solution was $LiPF_6$ (1 M) in a blend of linear and cyclic carbonates. The wound 4/5A-type cells were assembled in a dry room and filled with electrolyte in an argon-filled dry box. The power tests occurred in two steps. The first one consisted in two formation cycles at 60 °C at slow rate ($C/5$) between 2.7 and 4.1 V in order to assess the capacity (for NCA, a charge cut-off voltage of 4 V was chosen, in order to obtain similar capacity values). Then, the peak power test (PPT) procedure, according to a protocol well established for testing power abilities of batteries developed for EV and HEV [23], was used to evaluate discharge and charge powers at 30 °C and discharge power at −20 °C:

- at 30 °C, the cells were charged to 4.1 V (4 V for NCA) and then discharged at $C/5$ rate; during the discharge, a 20 s pulse was realized every 12 min at 20C rate until 2.5 V;
- at 30 °C, the cells were then charged at $C/5$ rate; a 10 s pulse was performed every 25 min at 9C rate until 4.2 V (4.1 V for NCA);
- finally, the cells were discharged at −20 °C, at $C/5$ rate; a 6 s pulse of 9C rate was performed every 25 min until 1.75 V with a 1 min standing period (open circuit) between pulses and continuous discharge. Note that the 20C pulses during the discharge correspond to acceleration periods whereas 9C pulses during the charge correspond to braking periods.

In order to compare the materials between them and to be free from any electrical problem in the cells, the power values were extrapolated from calculated resistance (R) and potential (U_0); these two parameters depended on changes in potential during the discharge (or during the charge) as well as during the pulses. The three following equations can be written:

During the discharge at 30 °C (resp. −20 °C) and charge at 30 °C:

$$U_{(C/5)} = U_0 - RI_{(C/5)} \quad (1)$$

During the discharge pulse at 30 °C:

$$U_{(20C)} = U_0 - RI_{(20C)} \quad (2)$$

During the charge pulse at 30 °C or discharge pulse at −20 °C:

$$U_{(9C)} = U_0 - RI_{(9C)} \quad (3)$$

with $I_{(C/5)}$, $I_{(20C)}$ and $I_{(9C)}$ values determined from the two formation cycles.

Change in power upon discharge at 30 °C was calculated 10s after the beginning of each pulse according to:

$$P_{\text{Discharge}(20C)} = U_{(20C)}I_{(20C)} = U_{(20C)}\frac{U_{(20C)} - U_o}{R} \quad \text{with}$$

$$I_{(20C)} = \frac{U_{(20C)} - U_o}{R} \quad (4)$$

Similarly, $P_{Charge(9C)}$ and $P_{Discharge(9C)}$ were calculated 2s after the beginning of each pulse, respectively at 30 °C and at −20 °C. The power results as obtained were normalized taking into account the electrode surface (~40 cm^2), to get the specific power in mW cm^{-2}.

The thermal stability of deintercalated "$Li_x(Ni_{0.40}Mn_{0.39}Co_{0.16}Al_{0.05})O_2$" was investigated by differential scanning calorimetry (Perkin Elmer Pyris Diamond DSC). Lithium cells were charged, after one cycle, to 4.5 V *vs.* Li^+/Li with a constant *C*/10 rate at room temperature. The positive electrodes as cycled were recovered from these cells in an argon-filled glove box, they were not washed and not dried before ~3 mg were sealed in a stainless steel pan closed with a gold plated copper seal. DCS analyses were then carried out at a scan rate of 10 °C min^{-1} from 50 °C to 450 °C. The results will be compared to those obtained with an industrial NCA material.

3. Results and discussion

3.1. Structural characterization

The X-ray diffraction pattern of "$Li(Ni_{0.40}Mn_{0.40}Co_{0.15}Al_{0.05})O_2$" is shown in Fig. 1. As expected, all the diffraction peaks could be indexed in the R-3 m space group according to the formation of an α-$NaFeO_2$ type lamellar oxide phase. The full width at half maximum of the main (0 0 3) and (1 0 4) diffraction lines is ~ 0.13° and shows the good crystallinity of the powder. The chemical composition of this sample was analyzed by ICP-OES titration and CHNS gas chromatography and was shown to be in fact $Li_{1.11}(Ni_{0.40}Mn_{0.39}Co_{0.16}Al_{0.05})_{0.89}O_2$ with a composition in transition metal ions close to the theoretical one, but with a Li/M ratio equal to 1.24 and thus significantly larger than the theoretical one (1.08). This lithium excess comes from the residual presence of LiOH after the formation and washing of the hydroxide. In the following "$Li(Ni_{0.40}Mn_{0.40}Co_{0.15}Al_{0.05})O_2$" will be associated to its actual composition $Li_{1.11}(Ni_{0.40}Mn_{0.39}Co_{0.16}Al_{0.05})_{0.89}O_2$. We considered this experimental composition for the refinement of the X-ray diffraction data by the Rietveld method, as described in detail elsewhere [15]. As shown also in Fig. 1, a very good agreement was obtained between the experimental and calculated X-ray diffraction profiles, with a good minimisation of the difference (Iobs. – Icalc.) and reliability factors of 3.5% and 13.9% for R_{Bragg} and R_{wp} respectively. The cation distribution was found to be $(Li_{0.98}Ni_{0.02})_{3b}(Li_{0.13}Ni_{0.34}Mn_{0.35}Co_{0.14}Al_{0.04})_{3a}(O_2)_{6c}$ with a small Li^+/Ni^{2+} exchange between the 3a and 3b sites. This low ion exchange between the 3a and 3b sites was expected as already discussed by some of us [15]: overlithiation induces for charge compensation the presence of 0.22 Ni^{3+} *vs.* 0.36 $Ni^{2+,3+}$ and thus a smaller Li^+/Ni^{2+} exchange between the slab and the interslab space (*vs.* the non-overlithiated composition). Indeed, Ni^{2+} and Li^+ cations are very similar in size (~0.70 Å) whereas Ni^{3+} and Li^+ are not [24].

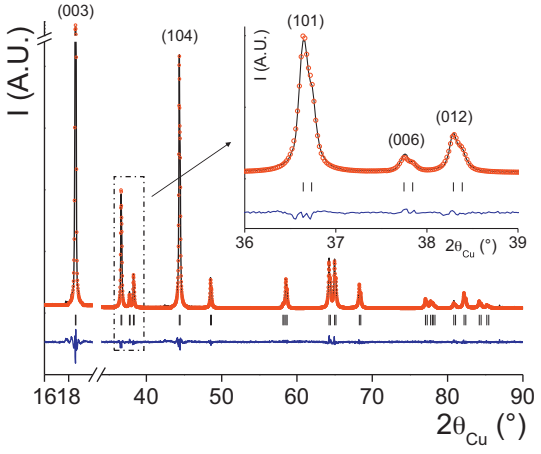

Fig. 1. Comparison of the experimental (○) and calculated (-) X-ray diffraction patterns for the $Li_{1.11}(Ni_{0.40}Mn_{0.39}Co_{0.16}Al_{0.05})_{0.89}O_2$ material. The difference (Iobs. – Icalc.) is also given. The angular range [90–120° (2θ)] is not given to enlarge the figure.

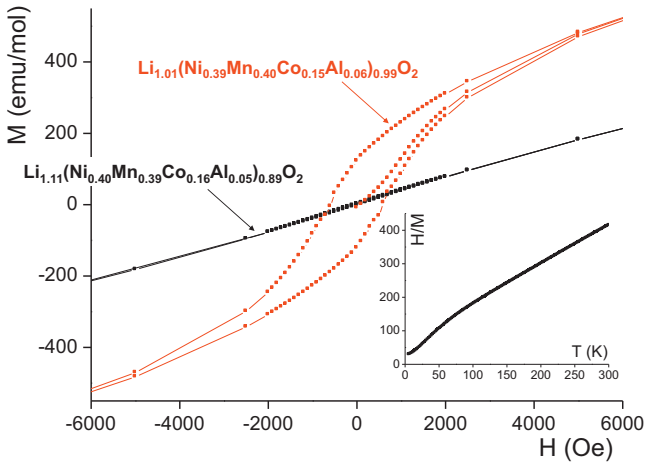

Fig. 2. Magnetization curve obtained at 5 K for $Li_{1.11}(Ni_{0.40}Mn_{0.39}Co_{0.16}Al_{0.05})_{0.89}O_2$ as a function of the magnetic field and compared to that of $Li_{1.01}(Ni_{0.39}Mn_{0.40}Co_{0.15}Al_{0.06})_{0.99}O_2$ [27]. In inset is given the thermal evolution of the H/M ratio for $Li_{1.11}(Ni_{0.40}Mn_{0.39}Co_{0.16}Al_{0.05})_{0.89}O_2$ (with H = 10 kOe).

As it was previously shown [15,25,26] for other nickel-rich lamellar oxides, magnetic properties are greatly affected by the presence of paramagnetic transition metal ions in the interslab space, and by their interaction with those from the slab. They are thus a tool of choice to support the composition and cation distribution of a layered oxide material. Fig. 2 shows the hysteresis loop *vs.* magnetic field obtained at 5 K for $Li_{1.11}(Ni_{0.40}Mn_{0.39}Co_{0.16}Al_{0.05})_{0.89}O_2$, in comparison with that of $Li_{1.01}(Ni_{0.40}Mn_{0.39}Co_{0.16}Al_{0.05})_{0.99}O_2$ obtained from a starting mixture with a small excess of LiOH and characterized by 0.08 Li^+/Ni^{2+} exchange between the slab and the interslab space [27]. As determined from the X-ray diffraction data analysis, the small amount of Ni^{2+} ions in the interslab space for $Li_{1.11}(Ni_{0.40}Mn_{0.39}Co_{0.16}Al_{0.05})_{0.89}O_2$ induces as expected only few magnetic interactions between the slab and the interslab space and explains thus the almost closed hysteresis loop (and a very small magnetization at zero field). In comparison, with an increase of the Li/Ni exchange as observed for $Li_{1.01}(Ni_{0.40}Mn_{0.39}Co_{0.16}Al_{0.05})_{0.99}O_2$, there is a significant residual magnetization at zero field and thus an opening of the hysteresis loop, those indicating formation of ferrimagnetic clusters whose size and number increase with the strong 180° Ni–O–Ni interactions between the paramagnetic Ni ions from the interslab space and from the slabs. The presence of a large amount of diamagnetic ions in the slab (~1/3 with 0.13 Li^+, 0.14 Co^{3+} and 0.04 Al^{3+}) participates also in the decreasing formation of ferrimagnetic clusters around the extra Ni^{2+} ions in the interslab space and in addition explains that antiferromagnetic interactions are predominant in this triangular lattice, as shown by the negative value observed for θp (−60 K). As shown in insert in Fig. 2, the thermal evolution of the H/M ratio is characteristic of a Curie–Weiss behaviour above 150 K for $Li_{1.11}(Ni_{0.40}Mn_{0.39}Co_{0.16}Al_{0.05})_{0.89}O_2$, the experimental Curie constant was found to be in good agreement with the theoretical one calculated from the composition (0.88 *vs.* 0.86). Magnetic measurements support thus the results obtained from chemical analyses and X-ray diffraction and confirm first, the composition of the layered oxide with a large overlithiation ratio and

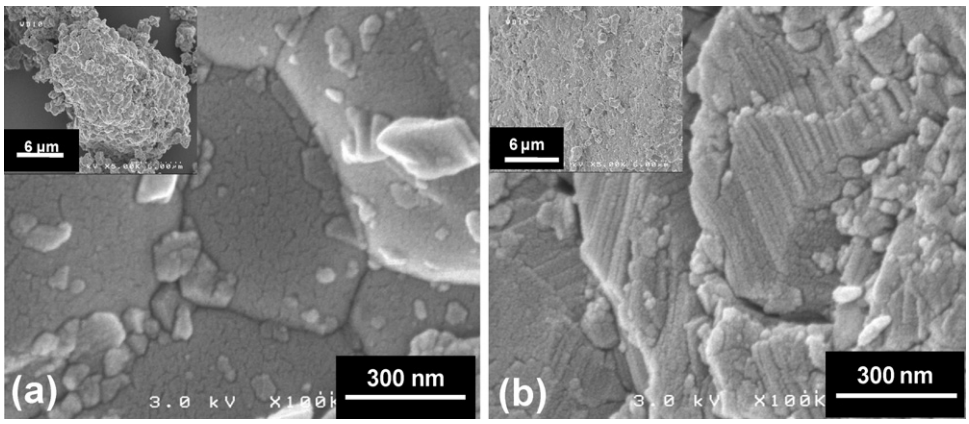

Fig. 3. Scanning electron micrographs obtained for different agglomerates of the $Li_{1.11}(Ni_{0.40}Mn_{0.39}Co_{0.16}Al_{0.05})_{0.89}O_2$ material.

second, the cation distribution with the formation of an almost 2D material.

The SEM results are shown in Fig. 3 for $Li_{1.11}(Ni_{0.40}Mn_{0.39}Co_{0.16}Al_{0.05})_{0.89}O_2$. The primary particles were heterogeneously distributed in size (between 100 nm and 1 μm in diameter, 500 nm in average) and in shape. As expected from the lithium excess used for synthesis and playing a role of flux, the agglomerates are mainly formed of sintered particles with a rounded shape (Fig. 3a) even if others are formed of laminated particles (Fig. 3b). In average, this powder shows dense agglomerates that should be in favour of good performances in power tests, as reported by Chen et al. [28].

3.2. Electrochemical performance

Fig. 4 shows changes in potential as a function of the lithium composition in $Li_{1.11}(Ni_{0.40}Mn_{0.39}Co_{0.16}Al_{0.05})_{0.89}O_2$ for laboratory lithium cells cycled at room temperature between 2.0 and 4.5 V (*vs.* Li^+/Li), at C/10 rate. The reversible capacity (125 mAh g^{-1} in discharge) obtained with $Li_{1.11}(Ni_{0.40}Mn_{0.39}Co_{0.16}Al_{0.05})_{0.89}O_2$ as positive electrode material in lithium cells is fair but smaller than that reported for example for $Li_{1.01}(Ni_{0.40}Mn_{0.39}Co_{0.16}Al_{0.05})_{0.99}O_2$ [27]. Polarization and irreversible capacity are similar for both, but the reversible capacity is smaller for $Li_{1.11}(Ni_{0.40}Mn_{0.39}Co_{0.16}Al_{0.05})_{0.89}O_2$ due to a larger overlithiation, an higher average oxidation state (d_M) for the transition metal ions (d_M = 3.26 *vs.* 3.02 for $Li_{1.01}(Ni_{0.40}Mn_{0.39}Co_{0.16}Al_{0.05})_{0.99}O_2$) and thus a smaller number of exchangeable electrons. Note that this composition was preferred for power tests due to an obvious larger tap density.

In order to perform tests such as those required for electric and hybrid vehicle applications 4/5A-type cells were built with graphite and $Li_{1.11}(Ni_{0.40}Mn_{0.39}Co_{0.16}Al_{0.05})_{0.89}O_2$ as negative and positive electrode materials, respectively. Fig. 5 compares at 60 °C their voltage evolution *vs.* capacity in galvanostatic mode at the constant *C*/5 rate in the 2.7–4.1 V potential range, compared to the industrial Ni-rich material (NCA) cycled at *C*/5 rate in the 2.7–4 V potential range. This NCA material showed, in a smaller potential window, slightly better discharge capacity (148 mAh g^{-1}) and less irreversible capacity (37 mAh g^{-1}) during this formation cycle than $Li_{1.11}(Ni_{0.40}Mn_{0.39}Co_{0.16}Al_{0.05})_{0.89}O_2$ (discharge capacity = 130 mAh g^{-1} and irreversible capacity = ~42 mAh g^{-1}). For that latter polarisation is similar to that observed in laboratory lithium cells (~100 mV) and slightly larger than for NCA (~70 mV). During the second formation cycle, the reversible capacity almost does not change with 128 mAh g^{-1} for $Li_{1.11}(Ni_{0.40}Mn_{0.39}Co_{0.16}Al_{0.05})_{0.89}O_2$ and 144 mAh g^{-1} for NCA, respectively.

For Li-ion cells targeting hybrid electric vehicle applications, discharge and charge power performances are very important technical objectives, and can typically be assessed as explained before by using 10s-PPT (peak power test) discharge and 2s-PPT

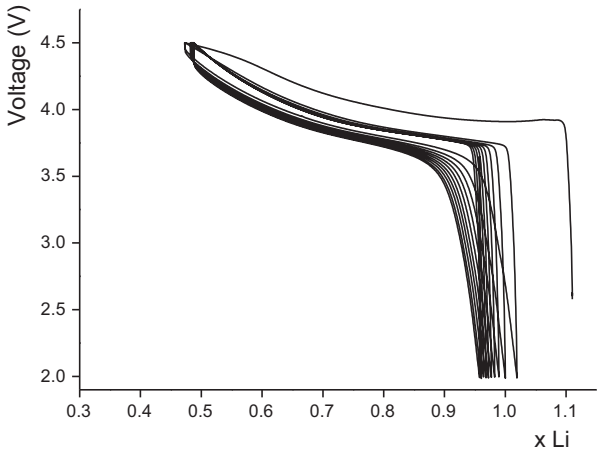

Fig. 4. Changes in potential as a function of the lithium content (x) during the first ten cycles of a lithium cell $Li//Li_x(Ni_{0.40}Mn_{0.39}Co_{0.16}Al_{0.05})_{0.89}O_2$ (galvanostatic mode, C/10 rate, 2–4.5 V potential window, room temperature).

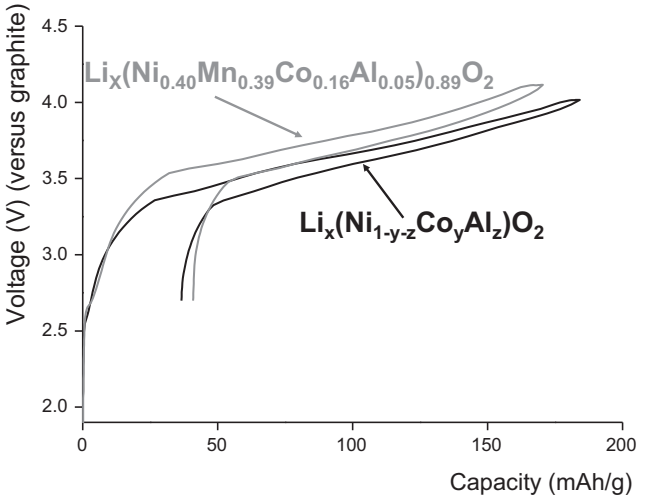

Fig. 5. Variation of the cell voltage *vs.* capacity during the first galvanostatic charge/discharge cycle for an 4/5A-type cell using $Li_{1.11}(Ni_{0.40}Mn_{0.39}Co_{0.16}Al_{05})_{0.89}O_2$ as positive electrode (and graphite as negative electrode), in comparison with that obtained for the industrial NCA material (at 60 °C and at *C*/5).

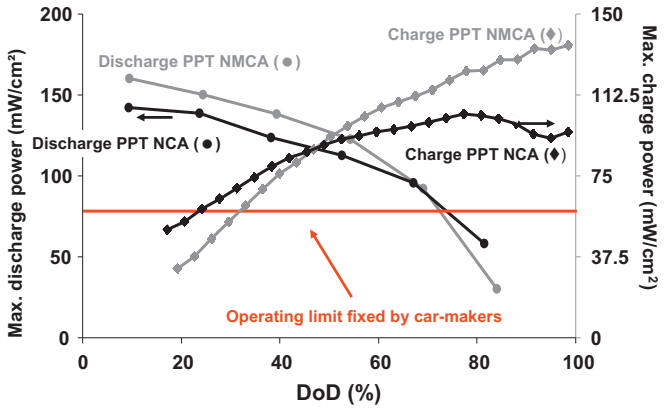

Fig. 6. Discharge and charge PPT results obtained at 30 °C at different depths of discharge (DODs) for the $Li_{1.11}(Ni_{0.40}Mn_{0.39}Co_{0.16}Al_{05})_{0.89}O_2$ material, in comparison with industrial NCA material.

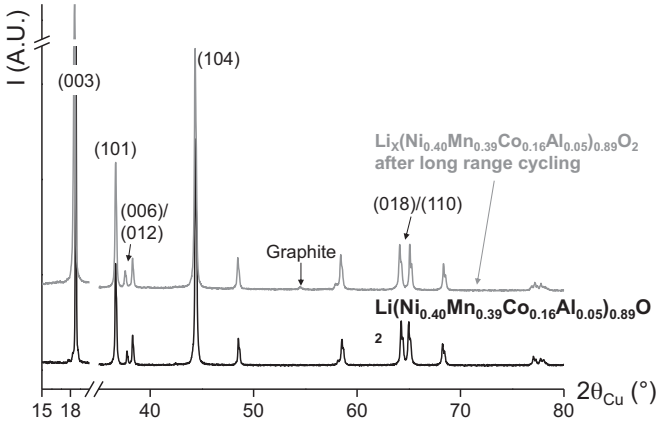

Fig. 8. X-ray diffraction pattern of the $Li_x(Ni_{0.40}Mn_{0.39}Co_{0.16}Al_{0.05})_{0.89}O_2$ material recovered after HEV cycling test, compared to that of the pristine material.

charge experiments. The electrochemical tests occur according to a well-established protocol (as described in the experimental part). Changes in discharge and charge power obtained at 30 °C as a function of the depth of discharge (or state of discharge, DOD) are shown in Fig. 6, for cells with $Li_{1.11}(Ni_{0.40}Mn_{0.39}Co_{0.16}Al_{0.05})_{0.89}O_2$ and NCA as positive electrode materials. The intersection between these two curves corresponds to the operating point and is close to 50% DOD. At 30 °C, the $Li_{1.11}(Ni_{0.40}Mn_{0.39}Co_{0.16}Al_{0.05})_{0.89}O_2$ material showed interesting power performance with a functional point of 125 mW cm^{-2} at 50% DOD, in comparison to 115 mW cm^{-2} at 47% DOD for NCA. These values are significantly larger than those defined as minimally required in discharge by car-makers before end of cell life, i.e. 80 mW cm^{-2}. Fig. 7 shows discharge power as a function of the DOD at −20 °C. At this temperature the power performance is similar for $Li_{1.11}(Ni_{0.40}Mn_{0.39}Co_{0.16}Al_{0.05})_{0.89}O_2$ and NCA, showing thus that whatever the temperature $Li_{1.11}(Ni_{0.40}Mn_{0.39}Co_{0.16}Al_{0.05})_{0.89}O_2$ shows power performances similar or even better than the industrial material NCA. As shown by these first very interesting results, further power tests upon long range cycling will have to be performed with an industrial $Li_{1.11}(Ni_{0.40}Mn_{0.39}Co_{0.16}Al_{0.05})_{0.89}O_2$ material and optimized electrodes.

Power evolution upon HEV cycling or microcycling (as described in USABC protocol, i.e. cycling at 40 °C, 20C and at 60% SOC and over a potential variation of 3% around 3.75 V) has been performed for $Li_{1.11}(Ni_{0.40}Mn_{0.39}Co_{0.16}Al_{0.05})_{0.89}O_2$. This cycling test has already shown that this laboratory synthesized

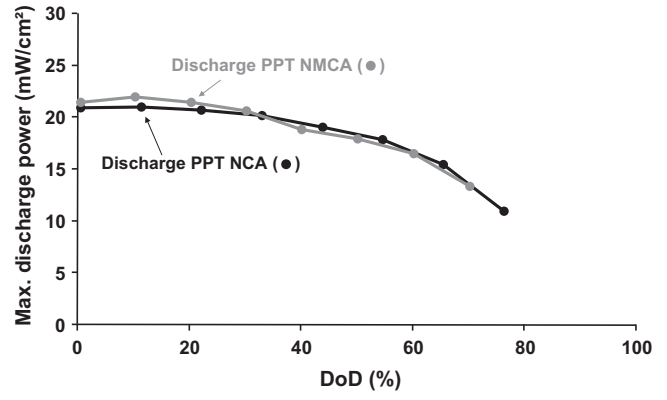

Fig. 7. Discharge PPT results obtained at −20 °C at different depths of discharge (DODs) for the $Li_{1.11}(Ni_{0.40}Mn_{0.39}Co_{0.16}Al_{05})_{0.89}O_2$ material, in comparison with the industrial NCA material.

$Li_{1.11}(Ni_{0.40}Mn_{0.39}Co_{0.16}Al_{0.05})_{0.89}O_2$ material delivers very interesting performance, because more than 60,000 microcycles could be done before reaching a value below the minimum power limit required by car-makers. As shown in Fig. 8, the X-ray diffraction pattern recorded for the material recovered after these long range power tests reveals no significant changes in the material, only a small broadening of the diffraction lines is observed (∼0.15° for (0 0 3) and (1 0 4) *vs.* ∼0.13° for the pristine material) suggesting limited change in its crystallinity. Scanning electron microscopy micrographs (Fig. 9) reveal no changes in the intergranular cohesion despite if primary particles appear more angular. Strains due

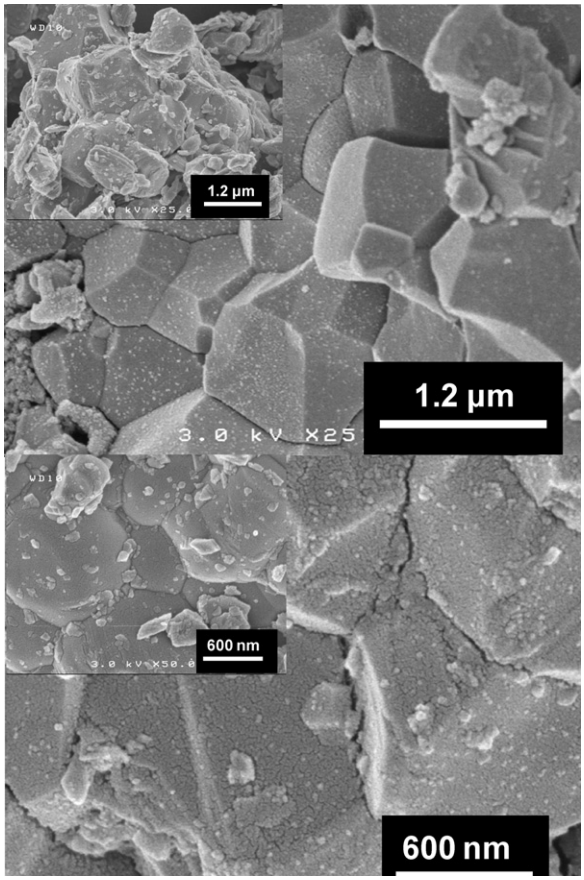

Fig. 9. Scanning electron micrographs (different zones) of the $Li_x(Ni_{0.40}Mn_{0.39}Co_{0.16}Al_{0.05})_{0.89}O_2$ material recovered after HEV cycling test.

Table 1
DSC results (onset temperature, exothermic peak temperature and energy of the exothermal reaction) obtained for the deintercalated material $Li_x(Ni_{0.40}Mn_{0.39}Co_{0.16}Al_{0.05})_{0.89}O_2$ compared to those obtained for industrial material NCA. These results were obtained after one cycle and a charge between 2.5 and 4.5 V *vs.* Li^+/Li at C/10 (4.4 V for NCA). The ratio $(Ni^{4+} + Co^{4+})/M$ and the amount of nickel (yNi_{3b}) present in the lithium site are also given.

Material	x in Li_xMO_2	$(Ni^{4+} + Co^{4+})/M$	yNi_{3b}	T_{onset} (°C)	T_{peak} (°C)	Energy ΔH (J g^{-1})
NCA ($LiNi_{1-y-z}Co_yAl_zO_2$)	0.37	0.66	/	200	275	−1385
$Li_x(Ni_{0.40}Mn_{0.39}Co_{0.16}Al_{0.05})_{0.89}O_2$	0.39	0.53	0.02	290	325	−490

to unit cell volume changes are limited for that kind of electrochemical tests because less than 1% volume changes are observed over the potential window 2.7–4.1 V [16]. Note for instance that the structural parameters determined for the material recovered in the discharged state after this long range cycling were $a = 2.8564(6)$ Å, $c = 14.282(4)$ Å and $V = 100.92(4)$ Å^3 *vs.* 2.8634(2), 14.245(2) and 101.15(2) respectively for the pristine material. These parameters are in good agreement with a smaller lithium content in the material after cycling, leading: (i) to more oxidized transition metal ions for charge compensation and thus to smaller metal–metal distance or $a_{hex.}$ parameter and, (ii) to larger electrostatic repulsion between the oxygen planes localized on one side and on the other side of the interslab space and finally to larger interslab distance and c_{hex}.

3.3. Thermal stability of the lithium deintercalated materials

The thermal stability of positive materials in the highly deintercalated state is a critical issue in judging their usefulness for practical batteries. Fig. 10 shows the differential scanning calorimetry (DSC) profiles for $Li_{1.11}(Ni_{0.40}Mn_{0.39}Co_{0.16}Al_{0.05})_{0.89}O_2$ compared to industrial NCA material, recovered from the lithium cells charged to 4.5 V (*vs.* Li^+/Li) after 1 cycle (4.4 V for the industrial material). The results (onset temperature, exothermic peak temperature and energy of the exothermal reaction) are summarized in Table 1 for the two samples. The exothermic reaction associated with the electrolyte and initiated by the decomposition of the deintercalated $Li_{1.11}(Ni_{0.40}Mn_{0.39}Co_{0.16}Al_{0.05})_{0.89}O_2$ starts at significantly higher temperature (onset temperature) in comparison with NCA (Fig. 10 and Table 1). Indeed, the onset temperature was ~290 °C for $Li_{1.11}(Ni_{0.40}Mn_{0.39}Co_{0.16}Al_{0.05})_{0.89}O_2$ and only 200 °C for NCA. In addition the temperature of the exothermal reaction (327 °C) is also significantly higher than that observed for the industrial material (275 °C). Finally the heat generation induced by the exothermic reaction is also much smaller than that obtained for the NCA material (reduced by three). The amounts of Ni^{4+} and Co^{4+} ions, those being unstable transition metal ions upon increasing temperature, are given in Table 1 for the two materials. Despite a similar capacity, industrial NCA shows a significantly larger amount of unstable cations, with in addition slightly higher 2D character (to the limit of the accuracy of the Rietveld refinement, 0 Ni in the Li site for NCA *vs.* 0.02 for $Li_{1.11}(Ni_{0.40}Mn_{0.39}Co_{0.16}Al_{0.05})_{0.89}O_2$), and is thus less stable than deintercalated $Li_{1.11}(Ni_{0.40}Mn_{0.39}Co_{0.16}Al_{0.05})_{0.89}O_2$ *vs.* temperature: oxygen is lost for a stabilization of the lithium deintercalated material through reduction of the transition metal ions and cation migration and reacts further through exothermic reactions with the carbonate solvents of the electrolyte [29].

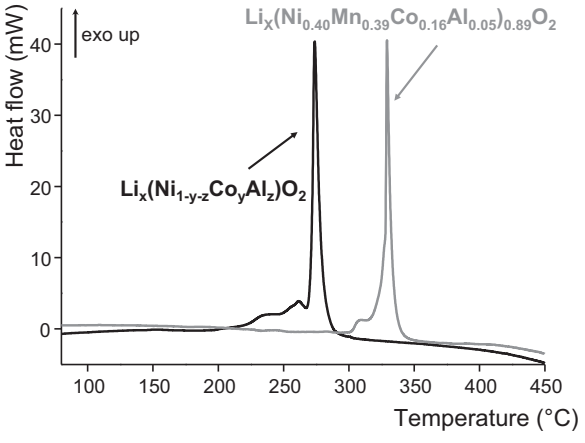

Fig. 10. DCS profiles obtained for the $Li_x(Ni_{0.40}Mn_{0.39}Co_{0.16}Al_{0.05})_{0.89}O_2$ and $Li_x(Ni_{1-y-z}Co_yAl_z)O_2$ materials recovered after one cycle and a charge between 2 and 4.5 V (4.4 V respectively) at C/10 rate. DSC profiles recorded at 10 °C min^{-1} for electrodes still wetted by the electrolyte (~2–3 mg).

4. Conclusion

$Li_{1.11}(Ni_{0.40}Mn_{0.39}Co_{0.16}Al_{0.05})_{0.89}O_2$ was prepared through the hydroxide route. Structural and physico-chemical characterizations have shown that this material is pure, with a large overlithiation ratio ($Li/M = 1.24$) inducing a small exchange ratio Li^+/Ni^{2+} between slabs and interslab spaces. This overlithiated material shows a heterogeneous distribution of particle sizes but dense agglomerates. This material, with a non-optimized synthesis, shows interesting electrochemical performance with: (i) promising results in power tests at 30 °C and −20 °C, (ii) structural stability after long range cycling at 40 °C and 20 °C in a small potential window and (iii) significantly improved thermal stability in the deintercalated state. In conclusion, this nickel and manganese-rich material shows power performance competitive with those of the industrial NCA material and in addition, a significantly improved thermal stability *vs.* industrial NCA: these properties make it very interesting for large scale batteries developed for transport applications.

Acknowledgements

The authors thank P. Dagault, C. Denage and L. Etienne from ICMCB for their technical assistance, C. Tessier (Saft) for fruitful discussions, and Région Aquitaine and Saft for financial support.

References

[1] J.-M. Tarascon, M. Armand, Nature 414 (2001) 359.
[2] I.B. Weinstock, J. Power Sources 110 (2002) 471.
[3] K. Amine, C.H. Chen, J. Liu, M. Hammond, A. Jansen, D. Dees, I. Bloom, D. Vissers, G. Henriksen, J. Power Sources 97–98 (2001) 684.
[4] C.H. Chen, J. Liu, M.E. Stoll, G. Henriksen, D.R. Vissers, K. Amine, J. Power Sources 128 (2004) 278.
[5] A.K. Padhi, K.S. Najundaswamy, J.B. Goodenough, J. Electrochem. Soc. 144 (1997) 1188.
[6] D.D. MacNeil, Z. Lu, Z. Chen, J.R. Dahn, J. Power Sources 108 (2002) 8.
[7] N. Ravet, S. Besner, M. Simoneau, A. Vallee, M. Armand, J.F. Patent No. EP1049182 (2000-05-02 2002), Magnan, CA.
[8] T. Ohzuku, Y. Makimura, Chem. Lett. 30 (2001) 744.
[9] J. Bréger, N. Dupré, P.J. Chupas, P.L. Lee, T. Proffen, J.B. Parise, C.P. Grey, J. Am. Chem. Soc. 127 (2005) 7529.
[10] T. Ohzuku, Y. Makimura, Chem. Lett. 30 (2001) 642.
[11] K. Amine, J. Liu, I. Belharouak, S.-H. Kang, I. Bloom, D. Vissers, G. Henriksen, J. Power Sources 146 (2005) 111.
[12] Y.B. He, Z.Y. Tang, Q.S. Song, H. Xie, Q.H. Yang, Y.G. Liu, G.W. Ling, J. Power Sources 185 (2008) 526.
[13] S.-H. Park, S.-H. Kang, I. Belharouak, Y.K. Sun, K. Amine, J. Power Sources 177 (2008) 177.
[14] M. Guilmard, C. Pouillerie, L. Croguennec, C. Delmas, Solid State Ionics 160 (2003) 39.

[15] N. Tran, L. Croguennec, C. Labrugère, C. Jordy, P. Biensan, C. Delmas, J. Electrochem. Soc. 153 (2006) A261.
[16] N. Tran, L. Croguennec, M. Ménétrier, F. Weill, Ph. Biensan, C. Jordy, C. Delmas, Chem. Mater. 20 (15) (2008) 4815.
[17] J. Bréger, F. Castaing, Ph. Biensan, J. Bains, L. Croguennec, C. Delmas, S. Levasseur, Patent FR 2937633; EP 2179968 (02/10/2009).
[18] F. Zhou, X. Zhao, Z. Lu, J. Jiang, J.R. Dahn, Electrochem. Commun. 10 (2008) 1168.
[19] F. Zhou, X. Zhao, J.R. Dahn, J. Electrochem. Soc. 156 (4) (2009) A343.
[20] Z. Lu, D.D. MacNeil, J.R. Dahn, Electrochem. Solid State Lett. 4 (2001) A200–A203.
[21] H.M. Rietveld, J. Appl. Cryst. 2 (1969) 65.
[22] J. Rodriguez-Carvajal, Laboratoire Léon Brillouin, http://www-llb.cea.fr/fullweb/powder.htm.
[23] USABC Electric Vehicle Battery Test Procedures Manual, Revision 2, DOE/ID-10479, January 1996; Freedom CAR Battery Test Manual For Power-Assist Hybrid Electric Vehicles, DOE/ID-11069, October 2003.
[24] R.D. Shannon, Acta Cryst. A32 (1976) 751.
[25] A. Rougier, C. Delmas, G. Chouteau, J. Phys. Chem. Solids 57 (1996) 1101.
[26] N.A. Chernova, M. Ma, J. Xiao, M.S. Whittingham, J.C. Jiménez, C.P. Grey, Mater. Res. Soc. Proc. 972 (2007) AA06.
[27] L. Croguennec, J. Bains, J. Bréger, C. Tessier, Ph. Biensan, S. Levasseur, C. Delmas, J. Electrochem. Soc. 158 (6) (2011) A664.
[28] C.H. Chen, J. Liu, M.E. Stoll, G. Henriksen, D.R. Vissers, K. Amine, J. Power Sources 128 (2) (2004) 278.
[29] M. Guilmard, L. Croguennec, C. Delmas, Chem. Mater. 15 (2003) 4484.